ELSEVIER

Journal of Crystal Growth 179 (1997) 297–308

JOURNAL OF CRYSTAL GROWTH

Numerical investigation of the effects of thermal creep in physical vapor transport

D.W. Mackowski*, V.R. Rao, D.G. Walker, R.W. Knight

Mechanical Engineering Department, Auburn University, Auburn, Alabama 36849, USA

Received 14 February 1996; accepted 27 November 1996

Abstract

It has been recently recognized that the nonisothermal conditions present in physical vapor transport ampoules can give rise to a slip flow of gas over the side walls of the ampoule. This phenomenon, known as thermal creep, is usually insignificant relative to buoyancy-induced flows under similar nonisothermal conditions, and has therefore been neglected in previous PVT numerical models. However, thermal creep can, in principle, become a dominant convection mechanism in buoyancy-free environments such as those encountered in microgravity experiments. We present here a numerical investigation of the effects of thermal creep on the growth process in axisymmetric, binary component PVT systems. A continuum-based model, which includes buoyancy and Soret diffusion, is developed. We show that thermal creep can result in recirculating bulk flows within the ampoule. For relatively high values of the Schmidt number and large wall temperature gradients, these flows can result in significantly nonuniform distributions of mass flux at the crystal interface, and can also be comparable to or exceed the flow velocities generated by buoyancy under normal gravity. The effects of thermal creep on buoyant convection, and on the Soret transport of the vapor, are examined.

PACS: 81.15; 02.60; 44.25

Keywords: Vapor transport; Numerical; microgravity; Heat transfer

1. Introduction

The formation of crystal structures is largely governed by the mass transport of the fluid material as it crystallizes at the nutrient/crystal interface [1]. This is certainly the case in physical vapor transport (PVT) crystal growth processes. In general, PVT is the process in which an amorphous solid is vaporized at one end of a closed, cylindrical ampoule, transported across the ampoule (usually through an inert carrier gas), and deposited onto a substrate that is maintained at a temperature lower than the source. The temperature and/or composition gradients that are invariably present in PVT processes can result in vapor transport that is dominated by buoyancy-induced convection. However, under microgravity (μg) environments

* Corresponding author. Fax: + 1 334 8443307.

PII S0022-0248(97)00087-0

the driving force behind buoyancy is largely eliminated and vapor transport occurs ostensibly in a diffusion-limited mode. Indeed, crystals grown in μg PVT experiments have been shown to possess uniquely different and improved structural properties than those grown on earth under similar operating conditions [2–4]. It is not known, however, to what extent the improvements result from modified vapor-phase transport conditions or the reduction in weight strain within the crystal.

Because of the considerable cost in performing μg PVT experiments, much effort has been given to numerical modeling of the process. Markham and Rosenberger [5] were the first to numerically examine the effects of microgravity on vapor transport rates in a cylindrical ampoule. Their results demonstrated that, under μg conditions, the transport of vapor is not adequately described by one-dimensional diffusion of the nutrient through a stagnant carrier fluid. Rather, the rejection of the carrier at the source and crystal interfaces leads to a recirculation of the carrier within the ampoule, which in turn results in radial concentration gradients of the nutrient. The effect of carrier recirculation and buoyant recirculation on growth rates and growth uniformity have been further examined in comprehensive numerical investigations of PVT by Greenwell [6], Markham et al. [7], and Nadarajah et al. [8].

In general, a key conclusion of the previous modeling efforts is that the elimination of buoyancy-induced convection results in improved uniformity of growth at the crystal interface. Recently, however, Rosner [9] reported that the nonisothermal conditions encountered in PVT processes can lead to additional, previously-unrecognized convection mechanisms. In particular, a temperature gradient tangential to a wall can result in a slip flow of gas over the wall. This phenomenon, which is known as thermal creep, is a macroscopic consequence of the molecular transfer of momentum to the wall. Molecules originating from the warmer regions in the gas will strike a wall with a higher momentum than those arriving from the cooler regions. The surface reacts to this uneven momentum transfer by imparting a force in the gas that is directed towards the warmer regions, which results in a slip flow over the surface. The velocity of the creep flow is constitutively related to the temperature gradient by [9–11]

$$u_c = \frac{C_s \nu}{T} \left.\frac{\partial T}{\partial z}\right|_{\text{wall}}, \tag{1}$$

where ν is the kinematic viscosity of the gas, z is the coordinate tangential to the wall, T is the gas temperature extrapolated to the wall, and C_s is a dimensionless coefficient which depends on the momentum and thermal accommodation of the molecule–wall collisions. For diffuse reflection of the molecules the value of C_s is estimated as 1.18 [10].

Under normal gravity conditions thermal creep typically results in a velocity that is significantly smaller than buoyancy-induced velocities produced under similar nonisothermal conditions [12]. In vanishing gravity, however, Rosner indicated that the creep velocity can become comparable to the typical diffusion velocity in PVT processes [9]. His conclusions were further supported by order-of-magnitude analyses by Napolitano et al. [13] and Viviani et al. [14].

As reported in these previous investigations, the ratio of the characteristic thermal creep and diffusion velocities will scale as

$$\frac{u_c}{u_D} \approx \frac{\mathrm{Sc}\,\Delta T}{T}, \tag{2}$$

in which $\mathrm{Sc} = \nu/D_{AB}$ is the Schmidt number, where ν and D_{AB} are the kinematic viscosity and binary diffusion coefficient, and T and ΔT are the characteristic temperature and temperature difference across the ampoule. Considering that $(\Delta T)/T$ cannot realistically exceed values of around 0.5 (and will most likely be around 0.05–0.1), the creep and diffusion velocities will be comparable only for the conditions of large Sc. This condition will be attained for vanishing concentration of the nutrient in the carrier and, simultaneously, relatively large ratios of the molecular weights of the nutrient and carrier. As noted in Refs. [9, 13, 14], there have been a number of μg experiments that fall into this regime – most notably the copper phthalocyanine experiments of Debe et al. [3].

The objective of this work is to use detailed numerical modeling to quantify the effects of

thermal creep on the PVT process. Since the conditions that are favorable to creep flows (i.e., large Sc and/or $(\Delta T)/T$) are also the conditions in which Soret (i.e., thermal) diffusion can become important, a second objective of the work is to examine the role of Soret diffusion (in combination with the thermal creep) on vapor transport. Emphasis is given to the effect of these transport mechanisms on the growth rates and growth uniformity at the crystal interface, and the differences in the growth patterns that occur with and without buoyancy.

2. Transport model

The geometry of the PVT ampoule is schematically illustrated in Fig. 1. The ampoule is cylindrical, with length L and radius R. Nutrient vapor, denoted as species A, originates from a planar source at $z = 0$ and deposits onto a planar crystal at $z = L$. The source and crystal interfaces are taken to be stationary, which is appropriate for the highly disparate vapor and solid-phase densities of the nutrient. We also neglect the effects of heat transfer within the source and crystal, and take both surfaces to be at the uniform temperatures of T_S and T_C, respectively. A constant mass of carrier gas, denoted as species B, resides within the ampoule and is completely rejected at all surfaces. The system is axisymmetric and in a steady-state.

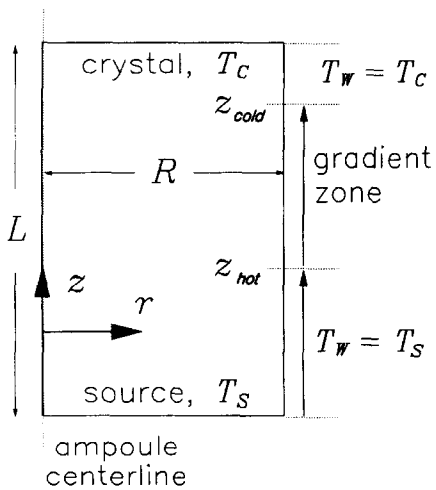

Fig. 1. Ampoule schematic.

Finally, we neglect the effects of temperature and composition on the thermal conductivity, diffusion coefficient, and kinematic viscosity, and take these properties to be constant.

To facilitate the identification of regimes in which creep and Soret mechanisms contribute to vapor transport, we adopt a nondimensional formulation of the governing equations. The velocities are normalized by the characteristic diffusion velocity D_{AB}/L, the temperature, pressure, and density of the gas are normalized by the values at the source, and the position variables are normalized with the ampoule length L. Denoting the nondimensional variables with the superscript *, the equations for mass, momentum, energy, and species conservation are

$$\nabla^* \cdot (\rho^* \boldsymbol{v}^*) = 0, \tag{3}$$

$$\nabla^* \cdot (\rho^* \boldsymbol{v}^* \boldsymbol{v}^*) = -N_P \nabla^* P^* + \mathrm{Sc}$$

$$\nabla^* \cdot [\nabla^* \boldsymbol{v}^* + (\nabla^* \boldsymbol{v}^*)^\dagger - \tfrac{2}{3} \boldsymbol{I} \nabla^* \cdot \boldsymbol{v}^*] + \rho^* g^* \hat{z}, \tag{4}$$

$$\nabla^* \cdot (\rho^* \boldsymbol{v}^* T^*) = \frac{\mathrm{Sc}}{\mathrm{Pr}} \nabla^* \cdot \nabla^* T^*, \tag{5}$$

$$\nabla^* \cdot (\rho^* \boldsymbol{v}^* w) = -\nabla^* \cdot \rho^* \boldsymbol{v}_A^*. \tag{6}$$

In the above, $\boldsymbol{v}^*$ is the nondimensional mass averaged velocity vector (with z and r components denoted as u and v), superscript $\dagger$ denotes transpose, $\boldsymbol{I}$ is the unit tensor, $\hat{z}$ is the unit vector in the z direction, and w is the mass fraction of the nutrient. The dimensionless parameters appearing in the momentum equation are defined

$$N_P = \frac{P_S L^2}{\rho_S D_{AB}^2}, \qquad g^* = \frac{g L^3}{D_{AB}^2}, \tag{7}$$

in which subscript S refers to the value at the source, and $\mathrm{Pr} = c_p \mu / k$ is the Prandtl number of the mixture. Note that the Schmidt number is defined with respect to the density at the source, i.e., $\mathrm{Sc} = \mu / \rho_S D_{AB}$, and the Rayleigh number for expansive/solutal buoyant convection is $\mathrm{Ra_L} = |(1 - \rho_C/\rho_S) g^*|/\mathrm{Sc}$. The nondimensional diffusion velocity of the nutrient, $\boldsymbol{v}_A^*$, is comprised of Fickian and Soret components. For dilute concentrations of the nutrient, the velocity is given by

$$\boldsymbol{v}_A^* = -\nabla w - \alpha_T \frac{w(1-w)}{T^*} \nabla T^*, \tag{8}$$

in which α_T denotes the Soret (or thermal diffusion) factor [1, 15, 16]. The corresponding cross-product transport mechanism in the energy equation, i.e., Dufour diffusion (enthalpy diffusion via a concentration gradient), has been neglected – which will be appropriate for the Pr/Sc conditions of interest. Likewise, we have neglected the contribution of temperature gradients to fluid stress ('thermal stress') in the momentum equations. Based on the order-of-magnitude estimates in Refs. [9, 13, 14], this mechanism will not significantly affect the flow field for the conditions examined here.

We assume ideal behavior of the gas in the ampoule. We also neglect the effects of flow-induced pressure gradients on the gas density – which is entirely reasonable for the low Reynolds number conditions (i.e., $\mathrm{Re} \sim 1$) that characterize our modeled PVT system. The density will then be a function solely of temperature and composition. In nondimensional form, the ideal gas law will then become

$$\rho^* = \frac{M^*}{T^*}, \tag{9}$$

with a nondimensional molecular mass of the mixture, M^*, given by

$$M^* = \frac{M}{M_S} = \frac{w_S(1 - N_M) + N_M}{w(1 - N_M) + N_M}, \tag{10}$$

where $N_M = M_A/M_B$ is the ratio of molecular masses of the nutrient and carrier.

Infinite-rate deposition kinetics are assumed at the source and crystal interfaces, which will correspond to fixed mole fractions of the nutrient at the interfaces for a given total pressure. We also neglect temperature jump between the solid and the gas, which is equivalent to assuming vanishingly small Knudsen number $\mathrm{Kn} = l/L$, where l is the mean-free-path of the gas molecules [17]. The boundary conditions at the source are then

$$T^*(r^*, 0) = 1, \tag{11}$$

$$w(r^*, 0) = \frac{N_M x_S}{1 + (N_M - 1)x_S}, \tag{12}$$

$$v^*(r^*, 0) = 0, \tag{13}$$

$$u^*(r^*, 0) = -\left(\frac{1}{1 - w}\frac{\partial w}{\partial z^*} + \frac{\alpha_T w}{T^*}\frac{\partial T^*}{\partial z^*}\right)_{z^*=0}, \tag{14}$$

in which x_S is the specified mole fraction of the nutrient at the source. Analogously, the boundary conditions at the crystal interface are

$$T^*(r^*, 1) = T_C^*, \tag{15}$$

$$w(r^*, 1) = \frac{N_M x_C}{1 + (N_M - 1)x_C}, \tag{16}$$

$$v^*(r^*, 1) = 0, \tag{17}$$

$$u^*(r^*, 1) = -\left(\frac{1}{1 - w}\frac{\partial w}{\partial z^*} + \frac{\alpha_T w}{T^*}\frac{\partial T^*}{\partial z^*}\right)_{z^*=1}, \tag{18}$$

where $T_C^* = T_C/T_S$.

The temperature distribution on the wall plays a key role in the magnitude and resulting effects of thermal creep. To provide a degree of freedom in choosing the temperature distribution – yet maintain a relatively simple form – we model the wall temperature in a piecewise-linear fashion. The distribution is described by two characteristic lengths; z_{hot} and z_{cold}. For wall positions between $z = 0$ and z_{hot}, the wall temperature is equal to the source temperature, between z_{hot} and z_{cold}, the wall temperature varies linearly from the source to the crystal temperature, and from $z = z_{cold}$ to L the wall temperature is equal to the crystal temperature. This distribution is somewhat representative of the three-zone arrangement employed in the NASA μg crystal growth furnace [18]. We also assume that deposition of the nutrient does not occur on the side wall. The boundary conditions on the side wall can then be stated in nondimensional form as

$$T^*(R^*, z^*) = \begin{cases} 1, & 0 \leqslant z^* \leqslant z_{hot}^* \\ 1 - (1 - T_C^*)\dfrac{z^* - z_{hot}^*}{z_{cold}^* - z_{hot}^*}, & z_{hot}^* < z^* < z_{cold}^* \\ T_C^*, & z_{cold}^* \leqslant z^* \leqslant 1 \end{cases} \tag{19}$$

$$\left(\frac{\partial w}{\partial r^*} + \alpha_T w(1 - w)\frac{\partial T^*}{\partial r^*}\right)_{r^*=R^*} = 0, \tag{20}$$

$$u^*(R^*, z^*) = \left.\frac{C_s \mathrm{Sc}}{\rho^* T^*}\frac{\partial T^*}{\partial z^*}\right|_{r^*=R^*}, \tag{21}$$

$$v^*(R^*, z^*) = 0, \tag{22}$$

in which $R^* = R/L$. At the centerline of the ampoule we impose the usual symmetry conditions,

which correspond to zero v^* and zero radial gradients of u^*, T^*, and w.

Solution of Eqs. (3)–(6) was accomplished using the SIMPLE algorithm as described by Patankar [19]. Discretization of the domain followed the staggered-grid procedure required by the SIMPLE method. A nonuniform grid was employed which concentrated grid points near the interfaces and walls of the ampoule. Typically, 33 grid points were used in the radial direction, and up to 53 grid points were used in the axial direction. In all the cases, the presented results for dimensionless velocities are within 0.5% of the values obtained when the number of grid points was doubled. Details of the solution method are given in Ref. [20].

3. Results and discussion

3.1. System parameters

The relevant dimensionless parameters include those pertaining to the fixed boundary conditions (x_S, x_C, T_C^*, z_{hot} and z_{cold}^*), those describing the thermophysical and transport properties of the mixture (Sc, Pr, C_s, α_T and N_M), and those describing the ampoule geometry and environment (R^* and g^*). The actual value of the pressure number N_P is irrelevant (provided it is a positive number) since we assume pressure gradients have no effect on density.

Fixed values of parameters used in this work are Pr = 0.7, $C_s = 1.18$, $z_{cold}^* = 1$, and $R^* = \frac{1}{5}$. The Soret factor α_T is set either to zero (no thermal diffusion) or to 3Sc/4, which represents the limiting value attained for a dilute concentration of a high-molecular-weight nutrient in a low-molecular weight carrier [16, 21].

It should be noted that, in principle, the ratio of nutrient mole fractions at-the source and crystal interfaces could be related to the temperature ratio via a Clausius–Clapeyron equation for the specific crystal material and ampoule's total pressure. We choose not to introduce such a relationship – since it would eliminate one parameter (e.g., x_C) by introducing another (the enthalpy of vaporization of the crystal). We treat the mole fractions and the temperatures as independent – yet attempt to assign values to them that are in the realm of physical plausibility.

3.2. Diffusive/thermal creep convective flows

We begin by examining the effect of thermal creep on the flowfield and interface flux in the absence of gravity and Soret diffusion. As a starting point, we consider a configuration that is somewhat representative of the H_2–I_2 system modeled in Refs. [5–8]. The molecular mass ratio is set to $N_M = 254/2 = 127$, and the source and crystal nutrient mole fractions are $x_S = 0.7$ and $x_C = 0.3$. The one-dimensional mass transfer Peclet number for this situation, which is defined [6]

$$\mathrm{Pe}_{1D} \equiv \frac{u_{1D}L}{D_{AB}} = \frac{w_C}{x_C} \ln\left(\frac{1 - x_C}{1 - x_S}\right), \tag{23}$$

is 1.2. We take the dimensionless crystal temperature to be $T_C^* = 350/400\ \mathrm{K} = 0.875$, which represents a somewhat larger temperature difference across the ampoule than those used in the previous investigations.

We focus first on the effects of an increasing creep velocity through the entire ampoule. To do this, we impose a linear wall temperature distribution from the source to the crystal (i.e., $z_{hot}^* = 0$ and $z_{cold}^* = 1$) and vary Sc from 1 to 10 while holding all other parameters constant. This is, of course, somewhat inconsistent with physics – because an increasing Sc would generally be associated with an increasing N_M and a decreasing nutrient vapor concentration. Our rationale for this approach, however, is that the next level of approximation would require an accounting of the effects of mixture composition on transport properties. We wish to avoid over-specifying the system – and keep the model simple to the maximum extent possible. We also note that for the buoyancy-free and Soret-free systems, the dimensionless velocity results are not appreciably altered by the value of N_M.

Fig. 2 shows the velocity field that results from the combined actions of the Stefan flow (or mass transfer-induced flow) and thermal creep at the side wall, with Sc = 1 on the left plot and 10 on the right. The scale of the vector arrows, which is the same in both plots, is presented in terms of the

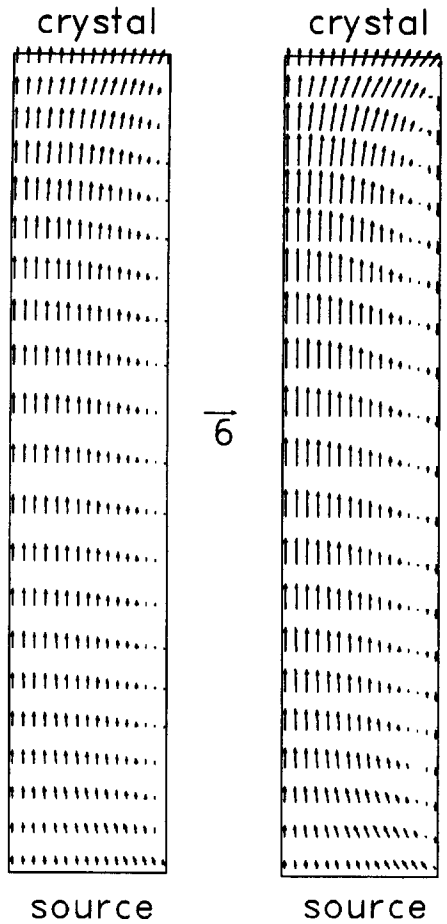

Fig. 2. Dimensionless velocity vectors for Sc = 1 (left) and Sc = 10 (right), for a linear temperature gradient across the entire ampoule side wall. Other model parameters described in the text. Origin of domain is lower left corner, velocity scale arrow is in terms of D_{AB}/L.

diffusion velocity D_{AB}/L. Note first that the case with Sc = 1 results in a velocity field that is practically indistinguishable from the zero-slip case. This is not surprising, because the ratio of characteristic creep and Stefan velocities, given by

$$\frac{u_c}{u_S} = \frac{u_c}{\mathrm{Pe} u_D} = \frac{\mathrm{Sc}\,\Delta T}{\mathrm{Pe}\,T}, \tag{24}$$

is approximately 0.2 for this case. Upon increasing Sc to 10, the creep velocity at the wall becomes comparable to the Stefan velocity. As expected [22], the combined effect results in a recirculating

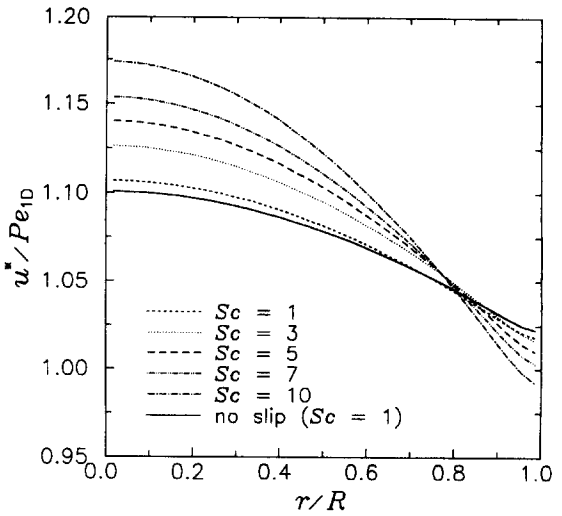

Fig. 3. Normalized interfacial velocities vs. dimensionless radial position r/R as a function of Sc, other conditions are the same as in Fig. 2.

flow, with the cold fluid pumped towards the source along the walls, and returning to the crystal along the ampoule centerline.

Even though thermal creep results in a roughly 50 percent increase in centerline velocity for Sc = 10, the total mass transfer rate to the crystal is only slightly increased (ca. 5%) by the creep-induced recirculation. The recirculating flow does, however, have a significant effect on the distribution of mass flux at the crystal interface. Shown in Fig. 3 are growth distributions as a function of radial position for Sc ranging from 1 to 10, with all other model conditions the same as in the previous plot. Also presented are the results for Sc = 1 with zero-slip boundary conditions at the walls. We present a normalized mass flux, which corresponds to the ratio of the dimensionless normal velocity at the interface divided by the 1-D Peclet number predicted from Eq. (23). For Sc = 1 the growth distribution is essentially unchanged from that attained in the absence of creep. The fact that the distribution is not completely uniform in this case is due to the recirculation of the carrier in the ampoule, as discussed in Ref. [6]. An increasing magnitude of the creep velocity, brought on by large values of Sc, augments the radial segregation of the nutrient concentration above the interface.

Centerline growth rates are seen to increase by roughly 15% for the given range of Sc, which are balanced by a decrease in growth at the edges of the interface.

A linearly decreasing wall temperature distribution throughout the entire ampoule is not representative of actual PVT conditions. Frequently, the wall is maintained at a temperature at or above the source temperature to a position just above the crystal interface – it is to prevent the parasitic nucleation of the nutrient onto the wall [8]. With regard to thermal creep, this effect would increase the temperature gradient – and resulting creep velocity – at the wall adjacent to the interface. To investigate this effect, we changed the location of z^*_{hot} to points progressively closer to the crystal while maintaining Sc = 5 and all other conditions the same as in the previous results. Plots of the velocity field for $z^*_{hot} = 0.75$ and 0.875 are given in Fig. 4. A vortex is now created within the ampoule section corresponding to the wall temperature gradient, which increases in intensity as the length of the section decreases. Growth distributions calculated for the changing wall temperature distributions are plotted in Fig. 5, with the same normalization used in Fig. 3. As can be seen, a steepening of the wall gradient leads to an increasingly nonuniform growth distribution – with the greatest effects occurring at the edges of the interface. The central factor here is that the creep-induced recirculation occurs directly above the interface – and thus has a direct influence on the transport of nutrient at the crystal–vapor boundary. This behavior could be significantly reduced or eliminated by minimizing the wall temperature gradient at the interface.

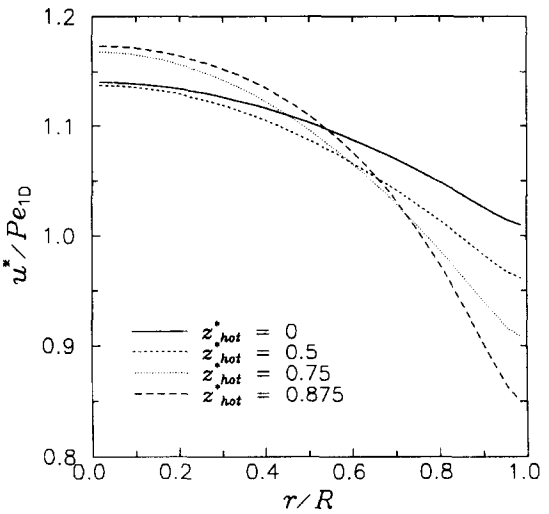

Fig. 5. Normalized interfacial velocities vs. dimensionless radial position as a function of z^*_{hot}, other conditions are the same as in Fig. 2.

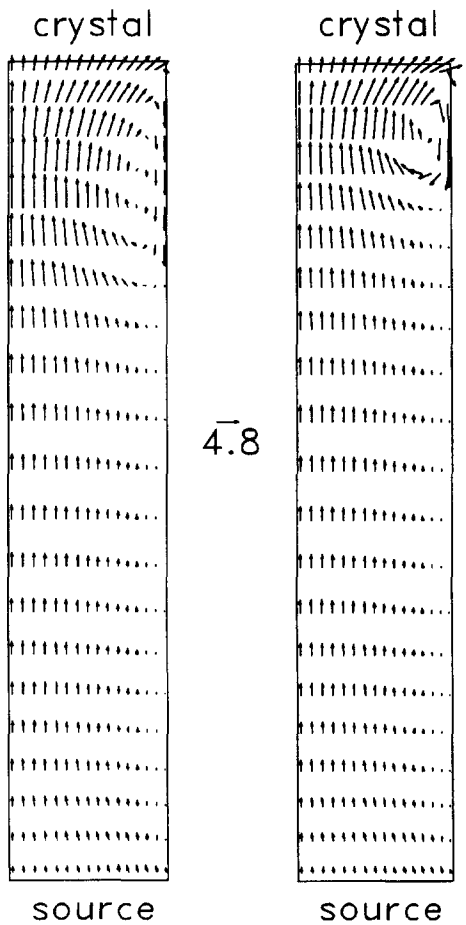

Fig. 4. Dimensionless velocity vectors for $z^*_{hot} = 0.75$ (left) and $z^*_{hot} = 0.875$ (right), with Sc = 5 and all other parameters are the same as in Fig. 2.

3.3. Thermal creep and Soret diffusion

The results of the previous section indicate that the creep flows will have bearing on vapor

transport only for relatively large Sc and small T_C^*. Large Sc values are typically associated with a large nutrient/carrier molecular mass ratio and a vanishingly small mass concentration of the nutrient in the gas – which will yield the maximum values of the Soret factor α_T. It is not surprising that the 'creep regime' would coincide with significant Soret transport of the vapor. Soret diffusion can be viewed as a molecular thermophoresis – especially in the limit of large nutrient molecules [15, 16]. Thermal creep at the wall and Soret transport of the vapor originate from the same fundamental mechanism – i.e., temperature gradients – and conditions which are favorable to one will be favorable to the other.

To model such conditions, we chose dimensionless parameters that were representative of the copper phthalocyanine PVT experiments conducted by Debe et al. [3]. Specifically, we used $T_C^* = 360/600\ \mathrm{K} = 0.6$, $x_S = 10^{-3}$, $x_C = 10^{-5}$, $N_M = 600/30 = 20$, Sc = 10 and $g^* = 0$. The one-dimensional Peclet number for this condition is $\mathrm{Pe}_{1D} \approx 0.02$. Information on the wall temperature distribution is not obtainable from Ref. [3]; we therefore considered separate cases in which the location of z_{hot}^* was moved from the source to the crystal.

Similar to the thermal creep, the effect of Soret diffusion on nutrient transport to the crystal is strongly dependent on the thermal boundary conditions of the side wall. Unlike mass transfer, heat is transferred to (and occasionally, from) the ampoule through the side walls. The temperature distribution in the gas – and its resulting effect on the concentration distribution via Soret diffusion – can therefore be highly two dimensional. To illustrate this behavior, we show in Fig. 6 contour plots of the nutrient mass fraction w in the ampoule, calculated without thermal creep, for different locations of z_{hot}^*. Labels on the contour lines represent the ratio w/w_S. For the low-Pe conditions used here, the linear temperature distribution ($z_{hot}^* = 0$) is closely representative of an adiabatic wall. Heat transfer for this case is essentially one-dimensional, and acts to transport the nutrient uniformly to the crystal. Note also that the mass fraction field for the $z_{hot}^* = 0$ case is qualitatively similar to that attained under high Pe, convective/diffusive conditions – in that the nutrient tends to 'pile up' at the crystal

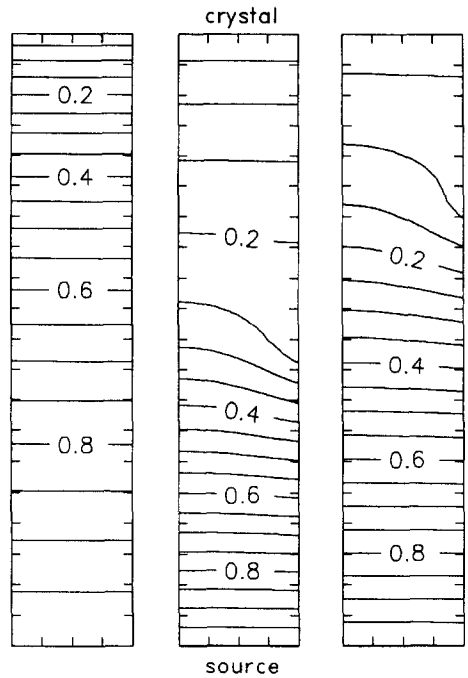

Fig. 6. Constant-value contours of w/w_S for $z_{hot}^* = 0$ (left), $z_{hot}^* = 0.5$ (middle), and $z_{hot}^* = 0.875$ (right). Zero-slip boundary conditions, diffusive and Soret transport of nutrient.

interface. Indeed, the processes of convection (via the Stefan flow) and Soret transport of nutrient are analogous for the given conditions. Within the bulk gas, nutrient transport is dominated by Soret diffusion. At the crystal, however, the contribution of Soret diffusion essentially vanishes (because of the relatively small mass fraction of nutrient at the crystal), and deposition becomes controlled by Fickian diffusion.

As z_{hot}^* is moved away from the source and towards the crystal, a progressively larger fraction of the heat that is transferred to the crystal originates from the heated side walls of the ampoule. This creates a two-stage effect within the mass fraction field. For regions well within the heated wall zone the temperature is nearly uniform at T_S. Nutrient transport therefore becomes controlled within this zone by the relatively slow process of Fickian diffusion – which results in the high-concentration gradients. At the transition point between the heated and gradient zones, radial heat transfer from

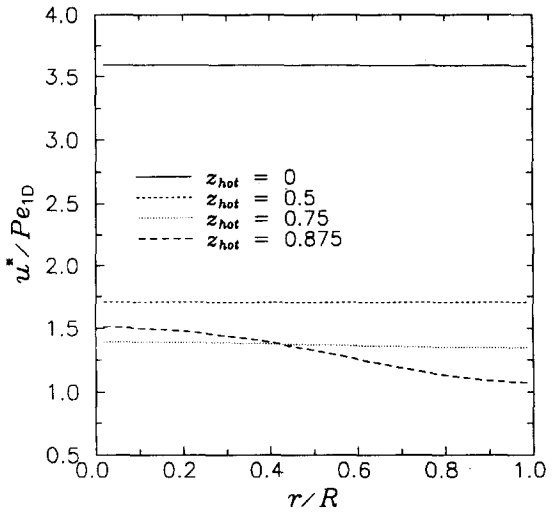

Fig. 7. Normalized interfacial velocities vs. dimensionless radial position as a function of z^*_{hot} for the conditions of Fig. 6.

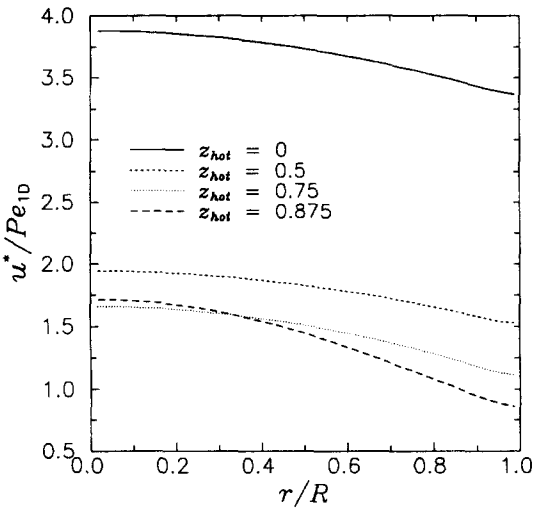

Fig. 8. Normalized interfacial velocities vs. dimensionless radial position for the conditions of Fig. 7, with the addition of thermal creep convection.

the wall acts to drive the nutrient towards the centerline. At the same time, the large axial temperature gradients within the gradient zone accelerate the transport of nutrient, which results in the low-concentration gradient within this second zone.

The radial segregation of the nutrient that results from the wall heat transfer can, as expected, have an effect on the flux distribution at the interface. This is demonstrated in Fig. 7, in which we plot the normalized interface velocities for different z^*_{hot} locations. Similar to the thermal creep effects discussed in Section 3.2, moving z^*_{hot} closer to the interface results in progressively nonuniform, axial-peaked growth distributions. The effect of Soret diffusion on the total mass transfer rate, on the other hand, is greatest for $z^*_{hot} = 0$ – since this condition results in an axial temperature gradient across the entire length of the ampoule.

For the given model conditions, the thermal creep velocity is on the order of 5 times greater than the characteristic diffusion velocity (see Eq. (2)). Consequently, including creep into the model results in an appreciable level of convective nutrient transport within the gradient section of the ampoule – as opposed to essentially convection-free conditions in the absence of creep. The recirculation generated by the creep has a significant effect on the distribution of flux at the interface, and the interfacial velocity profiles (shown in Fig. 8) attain a form that is qualitatively similar to those shown in Fig. 5. Soret diffusion, on the other hand, now affects primarily the overall mass transport to the interface. As was the case in the results of Section 3.2, inclusion of thermal creep has a relatively small effect on the total transfer of the nutrient.

3.4. Effect of creep on buoyant convection

The large Sc and large ΔT conditions in which creep becomes significant would correspond to conditions in which gas density is controlled primarily by temperature. It is therefore relevant to compare creep to buoyant flows that are driven by thermal expansion – as opposed to solutal-driven convection. To examine the interplay between buoyancy and creep, we performed calculations using the same conditions as in the previous section, except with $T^*_C = 0.8$ and $z^*_{hot} = 0.75$, and varied g^* from 0 to -5×10^7. The negative value of g^* indicates source-directed gravity, which represents the unstable configuration (for thermal expansion) of the crystal on the top. The equivalent Rayleigh number for the largest magnitude of g^* is 10^6. As a point of reference, an ampoule of 10 cm length, with $D_{AB} = 12.4\ cm^2/s$ (which corresponds

to the CuPc value used in Ref. [3] at 5.4 Torr total pressure) would have $g^* = -6.4 \times 10^3$ for unit gravity. Since D_{AB} varies inversely proportional to total pressure, the chosen range of g^* would represent operation of this experiment at total pressures up to about 0.6 atm.

Before presenting results of our calculations, we should note that the axisymmetric formulation of our model is of questionable validity for buoyant convection in vertical cylinder [7]. However, in the absence of thermal creep, the heated side walls of the ampoule would be expected to stabilize an initial axisymmetric buoyant recirculation as g^* decreases from zero. The gas, heated by the walls, would rise along the walls to the crystal and sink towards the source along the centerline. Beyond a critical value of $-g^*$ the axisymmetric pattern will become unstable and transform into a single, asymmetric roll. We performed a limited set of calculations to examine buoyant convection patterns, in which we used a two-dimensional cartesian model of the ampoule similar to that used in Ref. [8], with equivalent interface and side wall boundary conditions. Based upon these calculations, we estimate that the transformation from an axisymmetric convection pattern occurs for $-g^*$ in the range of 2×10^7–5×10^7.

A distinguishing feature between creep recirculation and expansive buoyant recirculation is that they occur in opposite directions. Creep drives the gas along the gradient section of the wall towards the source, whereas buoyancy is directed along the wall towards the crystal. The creep flow would thus be expected to inhibit the development of buoyant recirculation for this particular configuration. The interaction between creep and buoyant flows is graphically illustrated in Fig. 9, in which we present velocity vectors calculated for $g^* = -5 \times 10^5$ (left), -5×10^6 (middle), and -2×10^7 (right). The scale of the velocity vector, which is the same in all plots, is again given in terms of the diffusion velocity D_{AB}/L. At the smallest value of g^* the recirculation is completely dominated by the creep flow. At the next g^* level creep still controls the convection within the gradient zone, yet buoyancy is seen to have created a counter-rotating vortex directly below the creep-produced recirculation. Finally, increasing g^* to -2×10^7 results in an extremely

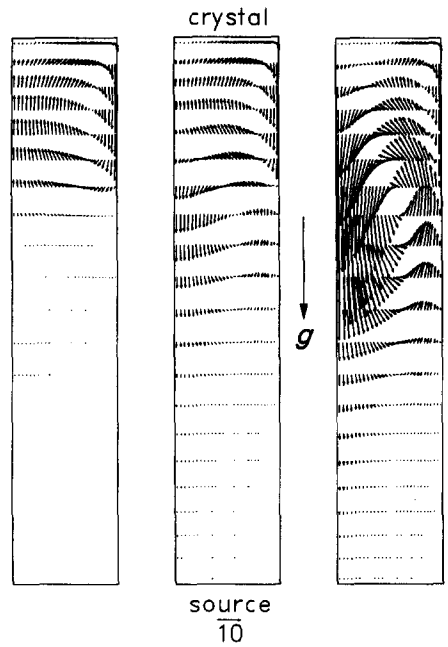

Fig. 9. Dimensionless velocity vectors for $g^* = -5 \times 10^5$ (left), -5×10^6 (middle), and -2×10^7 (right). Origin of domain is lower left corner.

complicated flow pattern. The upwards, buoyancy-controlled flow now extends to the crystal, and the creep-generated vortex has been pushed into a thin region adjacent to the side wall.

The transition from the creep to buoyancy controlled convection is reflected in the interfacial velocity profiles, which are shown in Fig. 10 for the same conditions as in Fig. 9. Also shown are the profiles calculated in the absence of thermal creep. The effect of combined creep and buoyant flows is seen to be qualitatively similar to that obtained by superimposing the separate velocity profiles for pure creep and pure buoyant convection. This behavior is somewhat expected. Even though the creep flow has a major effect on nutrient transport, the transport of energy and momentum are still controlled primarily by diffusion – for which a superposition of the independent creep and buoyant and flow fields becomes appropriate. This is further illustrated by examination of the total mass transfer rate to the crystal, denoted as j^*, as a function of g^*. We present this information in Fig. 11 for the zero-slip and thermal creep predictions, in

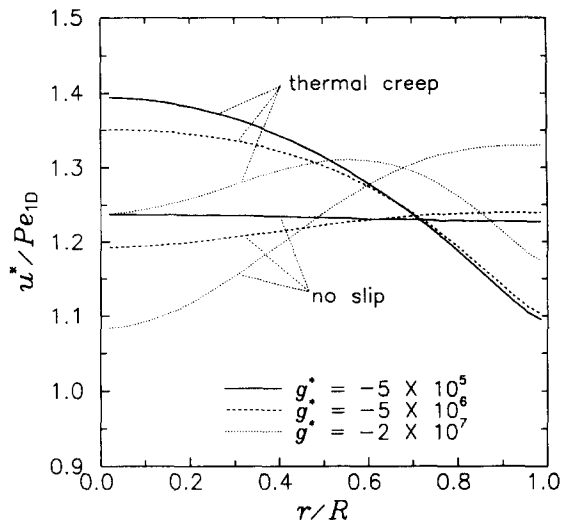

Fig. 10. Normalized interfacial velocities vs. dimensionless radial position as a function of g^*, for the thermal creep and zero-slip conditions.

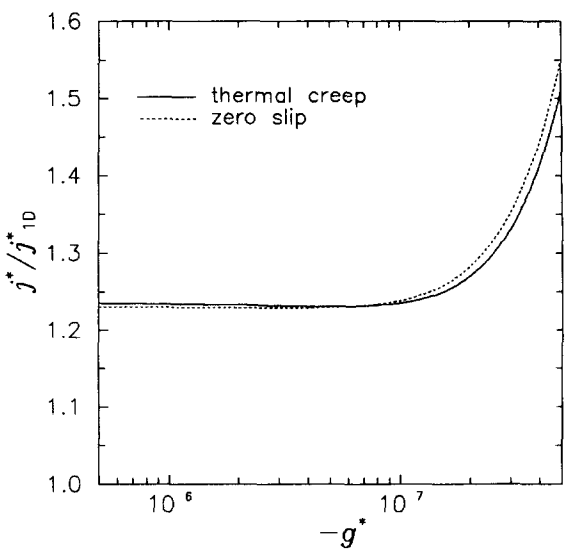

Fig. 11. Normalized total mass transfer rate vs. g^* for the thermal creep and zero-slip conditions.

which j^* has been normalized by $j^*_{1D} = \pi R^{*2} Pe_{1D}$. Thermal creep is seen to slightly delay the onset of buoyant convection control of mass transfer – which is indicated by the sudden increase in j^* near $g^* \approx -2 \times 10^7$ – yet for the most part the trends with and without thermal creep are similar.

Calculations were also performed, using the same conditions, of creep in conjunction with buoyancy stabilized (crystal on bottom) conditions. The results for this case show that the effects of creep are not appreciably altered by the presence of stabilized gravity relative to that calculated for zero gravity.

4. Summary

The results of this investigation reveal that, for certain operating conditions, thermal creep at the ampoule side walls can significantly re-distribute the mass flux arriving on PVT crystal interfaces. In general, the investigation supports the conclusions drawn from the order-of-magnitude estimates of Refs. [13, 14], in that the effects of creep become most evident for relatively large Sc, large ΔT and small Pe conditions. Indeed, flows resulting from normal-gravity buoyant convection can become, in this regime, relatively minor compared to the often-assumed 'higher-order' mechanism of thermal creep.

The model we have presented, however, is highly idealized, and is not meant for a precise prediction of growth processes in actual PVT experiments. The crystal interfaces in such experiments will not be isothermal because of latent heat release by the depositing vapor and finite conduction heat transfer resistance in the crystal [20, 23]. The interfaces will also not remain planar – especially in the presence of mechanisms (such as buoyancy, thermal creep and Soret diffusion) that tend to nonuniformly distribute the flux at the interface. Another uncertainty in the present analysis are the values of the slip coefficient on the side walls (C_s) and the Soret coefficient (α_T). Our model predictions used the theoretical maximum values of these properties, and consequently the actual effects of thermal creep and Soret diffusion will likely be smaller than those predicted here. Indeed, the validity of the continuum-based approach – with slip (and, possibly, jump) corrected boundary conditions – will be questionable for nonnegligible Kn and/or large $\Delta T/T$ conditions. Alternative approaches, such as those based upon Monte–Carlo simulations of gas molecular dynamics [24], are

needed to improve the understanding of mass transfer in such situations.

In closing, our results support previous conclusions [8], that the differences in structure between PVT crystals grown under normal and reduced gravitational conditions (Refs. [2–4]) cannot be attributed solely to the effects of gravity on vapor phase transport mechanisms. Because of the thermal creep, diffusion-limited transport of the vapor is not necessarily attained in buoyancy-free environments. Obviously, a better understanding of the effects of gravity on solid phase and interfacial mechanisms is needed to fully account for the differences. Nevertheless, our results strongly indicate that, as anticipated [9], the frequently-disregarded mechanism of thermal creep can have bearing on vapor transport – and should therefore be included in detailed, comprehensive modeling efforts of actual PVT processes.

Acknowledgements

This project has been supported by NASA-MSAD through Grant NAG8-977, Benjamin Penn, Contract Administrator. The authors have benefited from helpful discussions with Daniel Rosner.

References

[1] F. Rosenberger, Fundamentals of Crystal Growth (Springer, New York, 1979).
[2] H. Wiedemeier and D. Chandra, J. Crystal Growth 57 (1982) 159.
[3] M.K. Debe, R.J. Poirier, E.L. Cook, L.R. Miller, M.S. Spiering and S.P. Floeder, J. Vac. Sci. Technol. A 8 (1990) 49.
[4] L. van den Berg and W.F. Schnepple, Nucl. Instrum. Methods A 283 (1989) 335.
[5] B.L. Markham and F. Rosenberger, Chem. Eng. Commun. 5 (1980) 287.
[6] D.W. Greenwell, B.L. Markham and F. Rosenberger, J. Crystal Growth 51 (1980) 413.
[7] B.L. Markham, D.W. Greenwell and F. Rosenberger, J. Crystal Growth 51 (1980) 426.
[8] A. Nadarajah, F. Rosenberger and J.I.D. Alexander, J. Crystal Growth 118 (1992) 49.
[9] D.E. Rosner, Phys. Fluids A 1 (1989) 1761.
[10] L. Talbot, R.K. Cheng, R.W. Schefer and D.R. Willis, J. Fluid Mech. 101 (1980) 737.
[11] E.H. Kennard, Kinetic Theory of Gases, (McGraw-Hill, New York, 1938) p. 327–330.
[12] M. Vedha-Nayagam and D.W. Mackowski, J. Thermophys. Heat Transfer 6 (1992) 753.
[13] L.G. Napolitano, A. Viviani and R. Savino, Acta Astronautica 28 (1992) 197.
[14] A. Viviani and R. Savino, J. Crystal Growth 133 (1993) 217.
[15] D.E. Rosner, Physicochemical Hydrodynamics 1 (1980) 159.
[16] J.L. Castillo, P.L. Garcia and D.E. Rosner, J. Crystal Growth 116 (1991) 105.
[17] D.E. Rosner and D.H. Papadopoulos, I&EC Res. 35 (1996) 3210.
[18] Teledyne Brown Engineering, Document SP-DOC-6102, (1990).
[19] S.V. Patankar, Numerical Heat Transfer and Fluid Flow (McGraw-Hill, New York, 1980).
[20] D.W. Mackowski, V.R. Rao and R.W. Knight, J. Crystal Growth 165 (1996) 323.
[21] E.A. Mason, J. Chem. Phys. 27 (1957) 782.
[22] Ronser89.
[23] J.R. Abernathy, D.W. Greenwell and F. Rosenberger, J. Crystal Growth 47 (1979) 145.
[24] D.H. Papadopoulos and D.E. Rosner, Phys. Fluids 7 (1995) 2535.